Marder, E., and Gallen, S.F., 2023, Climate control on the relationship between erosion rate and fluvial topography: Geology, https://doi.org/10.1130/G50832.1

Supplementary Materials

- Text S1
- Figure and table captions
- Figures S1 to S7
- Tables S1, S2

Text S1

River profile analysis

For graded, steady-state river profiles, where the rock uplift rate, U, is balanced by the long term erosion rate, E, the relationship between local channel slope, S, and the upstream drainage area, A, can be described by a power function (Flint, 1974):

$$S = k_s A^{-\theta} \quad \text{(S1)},$$

where k_s is the channel steepness index, θ is the channel concavity index (Kirby and Whipple, 2012). The covariation of k_s and θ requires normalization that is typically done by fixing θ to a reference value (i.e., reference concavity index, θ_{ref}) that is ~0.3-0.7 globally to calculate the normalized channel steepness index k_{sn} (Kirby and Whipple, 2012; Lague, 2014; Harel et al., 2016). Equation S1 can be used to derive k_s or k_{sn} empirically from regression through S and A data. However, such calculation introduces noise and requires a large amount of smoothing (Snyder et al., 2000; Wobus et al., 2006). Thus, it is preferable to use χ, a path-dependent integral parameter of the inverse of A raised to θ_{ref} (Royden and Perron, 2013):

$$\chi = \int_{x_b}^{x} \left(\frac{A_0}{A(x')}\right)^{\theta_{ref}} dx' \quad \text{(S2)},$$

where x_b is the referenced distance at the drainage network outlet, and A_0 is the referenced upstream drainage area, usually chosen as unity ($A_0 = 1$). Equation S1, where $S = dz/dx$, can be integrated with respect to distance to generate a χ-elevation plot (typically referred to as a χ-plot):

$$z(x) = z(x_b) + k_{sn}\chi \quad \text{(S3)},$$

where the slope of a linear regression of $\chi - z$ is k_{sn}. We calculate χ by integrating A or drainage area weighted by the spatial distribution of mean annual precipitation, $MAP \times A$, in equation S2, using ChiProfiler (Gallen and Wegmann, 2017). We use χ and the precipitation-weighted χ to calculate k_{sn} and

k_{snQ} (cf. Adams et al., 2020), respectively, via linear regressions through basin-wide χ-z data (Equation S3; Fig. 1, inset in the main text). We calculate the R^2 for each of these linear regressions to determine the basin morphological steady state, where higher R^2 values reflect basins that appear to be morphologically in steady state (i.e., roughly linear χ-z plots; e.g., Fig. 1, inset in the main text), and low R^2 values reflect basins that are in a transient state of adjustment. We seek to avoid these transient basins because many bedrock rivers in them adjust their width in addition to slope during channel adjustment and affect assumed scaling relationships in the calculations above to bias the relationship between E and k_{sn} in equation 1 in the main text (e.g., Whittaker et al., 2007). We conduct this analysis for all basins with published ^{10}Be cosmogenic nuclide basin averaged erosion rates in detrital quartz from the Octopus archive (Codilean et al., 2018, 2022).

Binning, regressions, and sensitivity analyses

We use existing global climate data of mean annual precipitation (MAP), mean annual temperature (MAT) (Fick and Hijmans, 2017), aridity index (AI=MAP/Mean annual evapotranspiration) (Trabucco and Zomer, 2009), and SRTM 3-arc second digital elevation model (DEM) tiles (ME) (OpenTopography) to calculate mean climate proxy values for each basin (Figs. 1 in the main text, S1; Table S1). We convert all global data to rasters, project them to WGS 84 geographic coordinate system, and crop them to basin geometries using Arc Pro 2.0.8. We project the basin rasters to UTM coordinate system, resample them to 90 m cell size, calculate their mean MAP, MAT, AI, and ME values using Matlab and TopoToolbox (Schwanghart and Scherler, 2014), and compile this data with E, k_{sn}, and k_{snQ} data for each basin (Table S1). To control for bedrock variability, we restrict our analysis to bedrock rivers that drain ≥ 90% crystalline rocks (plutonic and metamorphic units) based on a global composite geological map (Fig. S2A; 'GLiM'; Hartmann and Moosdorf, 2012). We calculate the distribution and dominance of plutonic and metamorphic units and compare them to MAP, MAT, AI, and ME in each basin to ensure that there is no global relationship between rock type and climate variability (Fig. S2B; Table S1).

We bin the $E - k_{sn}$ and $E - k_{sn}Q$ datasets based on increments of MAP, MAT, AI, and ME (Fig. S3). We select the bins to have an equal number of data points, with at least 15 data points in each bin. For each climate bin, we conduct a linear regression through log-transformed $E - k_{sn}$ and $E - k_{snQ}$ data using total least squares to determine the power-law exponent, p, and its constant, C, in equation 1 (main text) (Fig. S4). We assess the relationships between these parameters and the climate proxy data to evaluate if systematic patterns exist (Fig. S4). We attempt to account for the general nonlinearity (i.e., p) in the global dataset by conducting normalized regressions through the data under a fixed p ~2.1 (i.e., the global value of our dataset; cf. Harel et al., 2016; Adams et al., 2020) to determine the normalized y-intercept, C_{ne} and C_{neQ}, for the $E - k_{sn}$ and $E - k_{snQ}$ data sets, respectively (Fig. S5; Table S2). For all modeled regressions, we calculate the statistical goodness-of-fit metrics of r-square, chi-square, and Kolmogorov-Smirnov two-sided p-value at the 90% significance level to evaluate the significance of p and C_{ne} in our analysis (Table S2). We calculate the uncertainties for p and C in each regression by conducting 10^5 Monte Carlo simulations, where each simulation is for a set of random realizations from E and k_{sn} or E and k_{snQ} and their standard error using a truncated normal distribution based for each data point (Figs. S3, S5; Table S2).

We conduct several sensitivity analyses to evaluate the robustness of p in our modeled regressions, namely testing the impact of the number of bins with an equal number of data points per bin (e.g., for the dataset in Table S1, 4 bins with 107 points per bin, 6 bins with 71 points per bin, 8 bins with 53 points per bin, etc.; Fig. S6A); testing for the impact of transience in our basin analysis by changing the minimum R^2 morphological threshold value from $R^2 = 0.75$ to $R^2 = 0.95$ (Figs. 1, inset in main text, S6B; Table S2); and testing for the impact of the chosen reference concavity index, by calculating k_{sn} under $\theta_{ref} = 0.3, 0.4$, and 0.5 (equation S2, S3; Fig. S6C). Generally, we find that p is robust to the number of bins and changes in θ_{ref} and that the increase of R^2 improve the overall fit for the modeled regressions (Table S2).

Threshold stochastic stream power incision models (STIMs) and discharge variability

Bedrock channel incision rate is often modeled as a function of the magnitude of the shear stress (or stream power) exerted on a river bed (Howard, 1994). Approximations of this general concept simulate the instantaneous channel incision rate, I^*, as a function of the channel slope, S, raised to an exponent n, upstream drainage area, A, raised to an exponent m, and an erodibility coefficient, K, which captures rock type, climate and changes in channel hydraulic geometry, and a term for threshold for channel incision, ψ (Lague et al., 2005; Lague, 2014):

$$I^* = KA^m S^n - \psi \tag{S4}$$

where $\psi = k_e {\tau_c}^a$, in which k_e and a are constants that depend on substrate properties and τ_c is the critical shear stress for channel incision. Assuming that ψ is negligible and that $I^* \cong E$ in steady-state basins (i.e., the instantaneous channel incision rate is steady over time and in equilibrium with the long-term basin-averaged erosion rate), equation S4 is reduced to the constant effective discharge stream power incision model (SPIM) solution (Howard, 1994; Kirby and Whipple, 2012; Lague, 2014):

$$E = KA^m S^n \quad \text{(S5).}$$

However, when the second right hand term in equation S4 is significant, the critical discharge needed to overcome the threshold shear stress, Q_c (which is typically defined by the effective bedload grain size), and the distribution of floods are important. Stochastic threshold stream power incision models (i.e., STIM) account for this via the calculation of E as the integral of the product of I (equation S4) and the probability of threshold-breaching floods (i.e., floods large enough to generate shear stress capable of exceeding ψ) for specific normalized discharges, $pdf\left(Q^*\right)$:

$$Q^* = Q/\overline{Q} \quad \text{(S6)}$$

$$E = \bar{I} = \int_{Q_c}^{Q_{max}} I^*\left(Q^*\right) pdf\left(Q^*\right) dQ \quad \text{(S7),}$$

where $\bar{I}$ is the river erosion rate, and Q, $\bar{Q}$, Q^*, and Q_{max} are the actual, mean, normalized, and maximum discharges, respectively (Lague et al., 2005; DiBiase and Whipple, 2011). Lague et al. (2005) present a model where $pdf\left(Q^*\right)$ is represented by an inverse gamma distribution:

$$pdf(Q^*) = \frac{k^{k+1}}{\Gamma(k+1)} exp\left(-\frac{k}{Q^*}\right) Q^{*-(2+k)} \quad \text{(S8),}$$

where Γ is the inverse gamma function, and k is a shape parameter that describes discharge variability. In this model, low to high k reflect heavier-tailed, higher-variability flood distributions to lighter-tailed, lower-variability flood distributions (Lague et al., 2005; Lague, 2014).

This model predicts that in threshold-dominated bedrock river systems, the nonlinearity between E and k_{sn} (equation 1 in main text) systematically increases with decreasing discharge variability (i.e., higher k in equation S8; Figure 4 in main text). This behavior arises because for steeper channels, smaller magnitude floods are capable of overcoming incision thresholds, while for shallow to moderate grade channels, small floods are less effective, allowing only larger floods to overcome bedrock incision thresholds (Lague et al., 2005; DiBiase and Whipple, 2011; Deal et al., 2018). The integral of discharge events that breach this incision threshold is related to the erosional efficiency in a STIM framework, where more threshold breaching events increase erosional efficiency (erosion rate at a given slope and drainage area). Thus, as channel steepness increases, the flood size needed to breach thresholds declines, and more erosive floods are included in a lighter-tailed, lower-discharge flood distribution relative to a heavier-tailed, higher-discharge flood distribution system.

To empirically determine k from discharge records, it is easier to use the complementary cumulative distribution function, $ccdf(Q^*)$, to avoid binning complexities when comparing actual discharge data (DiBiase and Whipple, 2011):

$$ccdf(Q^*) = \Gamma(k/Q^*, k+1) \qquad \text{(S9)}.$$

Empirical studies and theory suggest k to systematically increase with increasing MAP and AI (Lague, 2014; Rossi et al., 2016; Deal et al., 2018). To demonstrate this general pattern at the global scale, we use equation S9 along with several discharge records near some of our studied basins to empirically determine the shape parameter k for each of these stations and compare it with MAP and AI patterns. We gather mean daily discharge records of ~20-50 years from several gauges near some of our analyzed basins that span a large range of climate conditions to calculate their exceedance probability plots (Fig. S7A; see locations in Figs. 1 in main text, S1). We calculate similar exceedance probability plots using Lague et al.'s STIM and equation S9 to verify that STIM predictions generally fit the recorded data (Fig. S7B), and that predicted k values are consistent with MAP and AI patterns at these gauge stations (Fig. 4 in main text; Fig. S7C; DiBiase and Whipple, 2011; Lague, 2014; Deal et al., 2018).

Figure and table captions

Figure S1: Global climate rasters used for our analysis. **(A)** Mean annual precipitation (MAP; 'WorldClim 2'; Fick and Hijmans, 2017) **(B)** Mean annual temperature (MAT; 'WorldClim 2'; Fick and Hijmans, 2017); **(C)** Aridity index (AI; 'CGIAR-CSI'; Trabucco and Zomer, 2009); **(D)** Elevation (ME; 'ETOPO1'; Amanter and Eakins, 2009). Marked are locations of analyzed basin regions (red stars). IDH = Idaho, USA; DEN = Denver, USA; App = Appalachians, USA; SGM = San Gabriel Mountains, USA; GUA = Guatemala; TRI = Trinidad and Tobago; AND = Chilean/Bolivian Andes; BRA = Florianopolis, Brazil; ALPS = European Alps; SAF = South Africa; KEN = Kenya; NAM = Namibia; MAD = Madagascar; SIND = Southwest India; HIM = Himalayas; MYA = Myanmar; CHE = Chengdu, China; TAW = Taiwan; JAP = Japan; AUS = Australia.

Figure S2: **(A)** Global rock type data (after 'GLiM'; Hartmann and Moosdorf, 2012) classified by crystalline, volcanic, and sedimentary rocks, where crystalline rocks consist of plutonic and metamorphic units. All analyzed basins in this study consist of at least 90% crystalline units. **(B)** Binned data of the percentages of plutonic and metamorphic units for 428 basins under a steady state threshold of R^2> 0.9, versus MAP, MAT, AI, and ME (Table S1). At the global scale, no relationship is observed between changes in the percentage of plutonic or metamorphic units and climate.

Figure S3: **(A)** Modeled regressions for k_{sn} versus E (equation 1 in main text) for 428 basins under a steady state threshold of $R^2 > 0.9$, where each data point represents one basin. Data is classified and binned by (from top left clockwise) MAP, MAT, AI, and ME (see Table S1). Statistical goodness-of-fit parameters (R-square, chi-square, KS test p-value) for each climate bin modeled regression are summarized in Table S2. **(B)** Same as (A) but for k_{snQ}, where MAP across the basin is weighted in drainage area prior to calculation of χ (see text). Regressions with low or negative R-square or KS test p-value < 0.1 are dashed (see also Table S2). Inset figures show log-log plots of the main figures.

Figure S4: **(A)** Values of p in equation 1 for each modeled regression for k_{sn} and k_{snQ} under changes in MAP, MAT, AI, and ME. Note a systematic increase in p with increasing MAP (i.e., wetter) and AI (i.e., higher humidity). **(B)** Same as (A) but for C in equation 1. Note a systematic decrease in C with increasing MAP and AI. For all regressions, k_{snQ} does not significantly change systematic patterns. Most uncertainties in p and C are small and thus not visible.

Figure S5: **(A)** Modeled normalized regressions for k_{sn} versus E (equation 1 in main text) under a fixed p = 2.1, which is the global value from best fit regression through the entire E - k_{sn} dataset. Regressions and associated data points with low or negative R-square or p-value < 0.1 are dashed (see also Table S2). **(B)** Changes in C_{ne} and C_{neQ} under a fixed p = 2.1. Note that C_{ne}/C_{neQ} decreases over a small range ~1-8 X $10^{-9}yr^{-1}$ with all climate proxies. Inset figures show log-log plots of the main figures.

Figure S6: Sensitivity analyses for modeled regressions under **(A)** changes of the number of bins; **(B)** changes of the R^2 threshold used to define morphological steady state (e.g., Figure 1, inset in main text); **(C)** changes in θ_{ref}. p (and hence C that covary with it; Figure S4) is statistically robust to changes in MAP and AI under different number of bins, R^2 threshold values, and θ_{ref} values. Inset figures in (A) and (B) show all p values (i.e., also ones that are > 5).

Figure S7: **(A)** Exceedance probability plots of recorded mean daily discharge (m^3/s), Q (equation S6), from six stream gauge stations with records spanning ~20-50 yrs near some of our analyzed basins (for locations, see Figs. 1 in main text, S1). **(B)** Exceedance probability plots following equation S9, where low to high k represents high to low discharge variability (Lague et al., 2005; DiBiase and Whipple, 2011; Deal et al., 2018). Note a general systematic decrease in discharge variability (higher k) with increasing MAP and AI. **(C)** Scatter plot of MAP and AI as a function of calculated k in (B).

Table S1: Locations, climate proxy values, erosion rates, k_{sn}, $k_{sn}Q$, basin area, and percentage of crystalline units for 428 analyzed basins under a morphological steady-state threshold of $R^2 > 0.9$.

Table S2: p, C, C_{ne} and statistical goodness-of-fit metrics of R-square, chi-square, and Kolmogorov-Smirnov two-sided p-value at the 90% significance level for six climate bins of MAP, MAT, AI, and ME under different R^2 morphological steady-state thresholds from 0.75 to 0.95. Marked in red are low or negative r-square values or Kolmogorov-Smirnov p-value < 0.1 of poorly fit regressions.

References

Adams, B.A., Whipple, K.X., Forte, A.M., Heimsath, A.M., and Hodges, K.V., 2020, Climate controls on erosion in tectonically active landscapes: Science Advances, v. 6, p. eaaz3166, doi:10.1126/sciadv.aaz3166.

Amanter, C., and Eakins, B.W., 2009, ETOPO1 arc-minute global relief model: procedures, data sources and analysis.: National Centers for Environmental Information.

Codilean, A.T. et al., 2022, OCTOPUS Database v.2: Geology and geochemistry preprint, doi:10.5194/essd-2022-50.

Codilean, A.T., Munack, H., Cohen, T.J., Saktura, W.M., Gray, A., and Mudd, S.M., 2018, OCTOPUS: an open cosmogenic isotope and luminescence database: Earth System Science Data, v. 10, p. 2123–2139, doi:10.5194/essd-10-2123-2018.

Deal, E., Braun, J., and Botter, G., 2018, Understanding the Role of Rainfall and Hydrology in Determining Fluvial Erosion Efficiency: Journal of Geophysical Research: Earth Surface, v. 123, p. 744–778, doi:10.1002/2017JF004393.

DiBiase, R.A., and Whipple, K.X., 2011, The influence of erosion thresholds and runoff variability on the relationships among topography, climate, and erosion rate: Journal of Geophysical Research, v. 116, p. F04036, doi:10.1029/2011JF002095.

Fick, S.E., and Hijmans, R.J., 2017, WorldClim 2: new 1-km spatial resolution climate surfaces for global land areas: International Journal of Climatology, v. 37, p. 4302–4315, doi:10.1002/joc.5086.

Flint, J.J., 1974, Stream gradient as a function of order, magnitude, and discharge: Water Resources Research, v. 10, p. 969–973, doi:10.1029/WR010i005p00969.

Gallen, S.F., and Wegmann, K.W., 2017, River profile response to normal fault growth and linkage: an example from the Hellenic forearc of south-central Crete, Greece: Earth Surface Dynamics, v. 5, p. 161–186, doi:10.5194/esurf-5-161-2017.

Harel, M.-A., Mudd, S.M., and Attal, M., 2016, Global analysis of the stream power law parameters based on worldwide 10 Be denudation rates: Geomorphology, v. 268, p. 184–196, doi:10.1016/j.geomorph.2016.05.035.

Hartmann, J., and Moosdorf, N., 2012, The new global lithological map database GLiM: A representation of rock properties at the Earth surface: Geochemistry, Geophysics, Geosystems, v. 13, doi:10.1029/2012GC004370.

Howard, A.D., 1994, A detachment-limited model of drainage basin evolution: Water Resources Research, v. 30, p. 2261–2285, doi:10.1029/94WR00757.

Kirby, E., and Whipple, K.X., 2012, Expression of active tectonics in erosional landscapes: Journal of Structural Geology, v. 44, p. 54–75, doi:10.1016/j.jsg.2012.07.009.

Lague, D., 2014, The stream power river incision model: evidence, theory and beyond: Earth Surface Processes and Landforms, v. 39, p. 38–61, doi:10.1002/esp.3462.

Lague, D., Hovius, N., and Davy, P., 2005, Discharge, discharge variability, and the bedrock channel profile: Journal of Geophysical Research: Earth Surface, v. 110, p. n/a-n/a, doi:10.1029/2004JF000259.

Perron, J.T., and Royden, L., 2013, An integral approach to bedrock river profile analysis: Earth Surface Processes and Landforms, v. 38, p. 570–576, doi:10.1002/esp.3302.

Rossi, M.W., Whipple, K.X., and Vivoni, E.R., 2016, Precipitation and evapotranspiration controls on daily runoff variability in the contiguous United States and Puerto Rico: Journal of Geophysical Research: Earth Surface, v. 121, p. 128–145, doi:10.1002/2015JF003446.

Royden, L., and Taylor Perron, J., 2013, Solutions of the stream power equation and application to the evolution of river longitudinal profiles: Journal of Geophysical Research: Earth Surface, v. 118, p. 497–518, doi:10.1002/jgrf.20031.

Schwanghart, W., and Scherler, D., 2014, Short Communication: TopoToolbox 2 – MATLAB-based software for topographic analysis and modeling in Earth surface sciences: Earth Surface Dynamics, v. 2, p. 1–7, doi:10.5194/esurf-2-1-2014.

Snyder, N.P., Whipple, K.X., Tucker, G.E., and Merritts, D.J., 2000, Landscape response to tectonic forcing: Digital elevation model analysis of stream profiles in the Mendocino triple junction region, northern California: Geological Society of America Bulletin, v. 112, p. 1250–1263.

Trabucco, A., and Zomer, R.J., 2009, Global aridity index (global-aridity) and global potential evapo-transpiration (global-PET) geospatial database.: CGIAR Consortium for Spatial Information, v. 89, p. 1–2.

Whipple, K.X., Forte, A.M., DiBiase, R.A., Gasparini, N.M., and Ouimet, W.B., 2017, Timescales of landscape response to divide migration and drainage capture: Implications for the role of divide mobility in landscape evolution: Landscape Response to Divide Mobility: Journal of Geophysical Research: Earth Surface, v. 122, p. 248–273, doi:10.1002/2016JF003973.

Whittaker, A.C., Cowie, P.A., Attal, M., Tucker, G.E., and Roberts, G.P., 2007, Bedrock channel adjustment to tectonic forcing: Implications for predicting river incision rates: Geology, v. 35, p. 103, doi:10.1130/G23106A.1.

Willett, S.D., McCoy, S.W., Perron, J.T., Goren, L., and Chen, C.-Y., 2014, Dynamic Reorganization of River Basins: Science, v. 343, p. 1248765–1248765, doi:10.1126/science.1248765.

Wobus, C., Whipple, K.X., Kirby, E., Snyder, N., Johnson, J., Spyropolou, K., Crosby, B., and Sheehan, D., 2006, Tectonics from topography: Procedures, promise, and pitfalls, *in* Tectonics, Climate, and Landscape Evolution, Geological Society of America, doi:10.1130/2006.2398(04).

Fig. S1

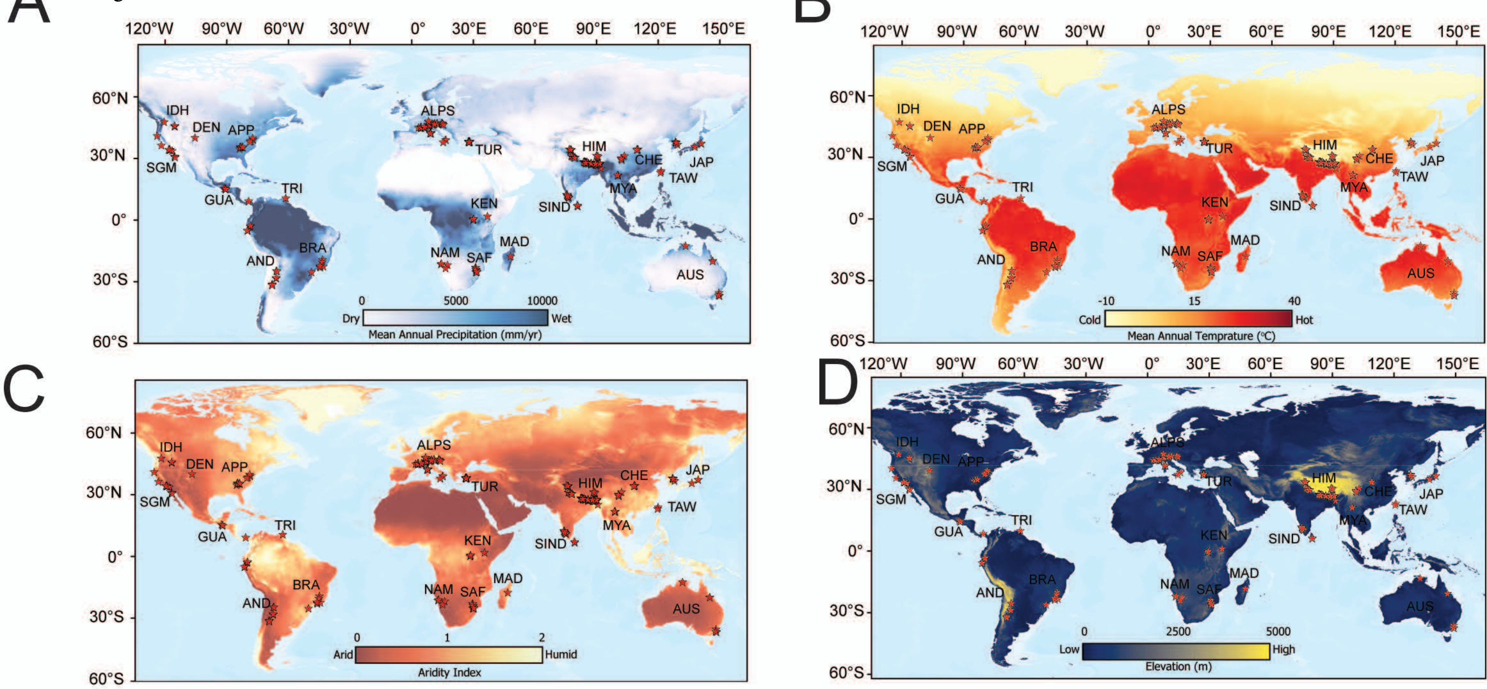
A
120°W 90°W 60°W 30°W 0° 30°E 60°E 90°E 120°E 150°E
60°N 30°N 0° 30°S 60°S
IDH DEN APP SGM GUA TRI AND BRA ALPS TUR KEN NAM SAF MAD HIM CHE JAP TAW MYA SIND AUS
0 5000 10000
Dry Wet
Mean Annual Precipitation (mm/yr)
B
120°W 90°W 60°W 30°W 0° 30°E 60°E 90°E 120°E 150°E
60°N 30°N 0° 30°S 60°S
IDH DEN APP SGM GUA TRI AND BRA ALPS TUR KEN NAM SAF MAD HIM CHE JAP TAW MYA SIND AUS
-10 15 40
Cold Hot
Mean Annual Temprature (°C)
C
60°N 30°N 0° 30°S 60°S
IDH DEN APP SGM GUA TRI AND BRA ALPS TUR KEN NAM SAF MAD HIM CHE JAP TAW MYA SIND AUS
0 1 2
Arid Humid
Aridity Index
D
120°W 90°W 60°W 30°W 0° 30°E 60°E 90°E 120°E 150°E
60°N 30°N 0° 30°S 60°S
IDH DEN APP SGM GUA TRI AND BRA ALPS TUR KEN NAM SAF MAD HIM CHE JAP TAW MYA SIND AUS
0 2500 5000
Low High
Elevation (m)

Fig. S2

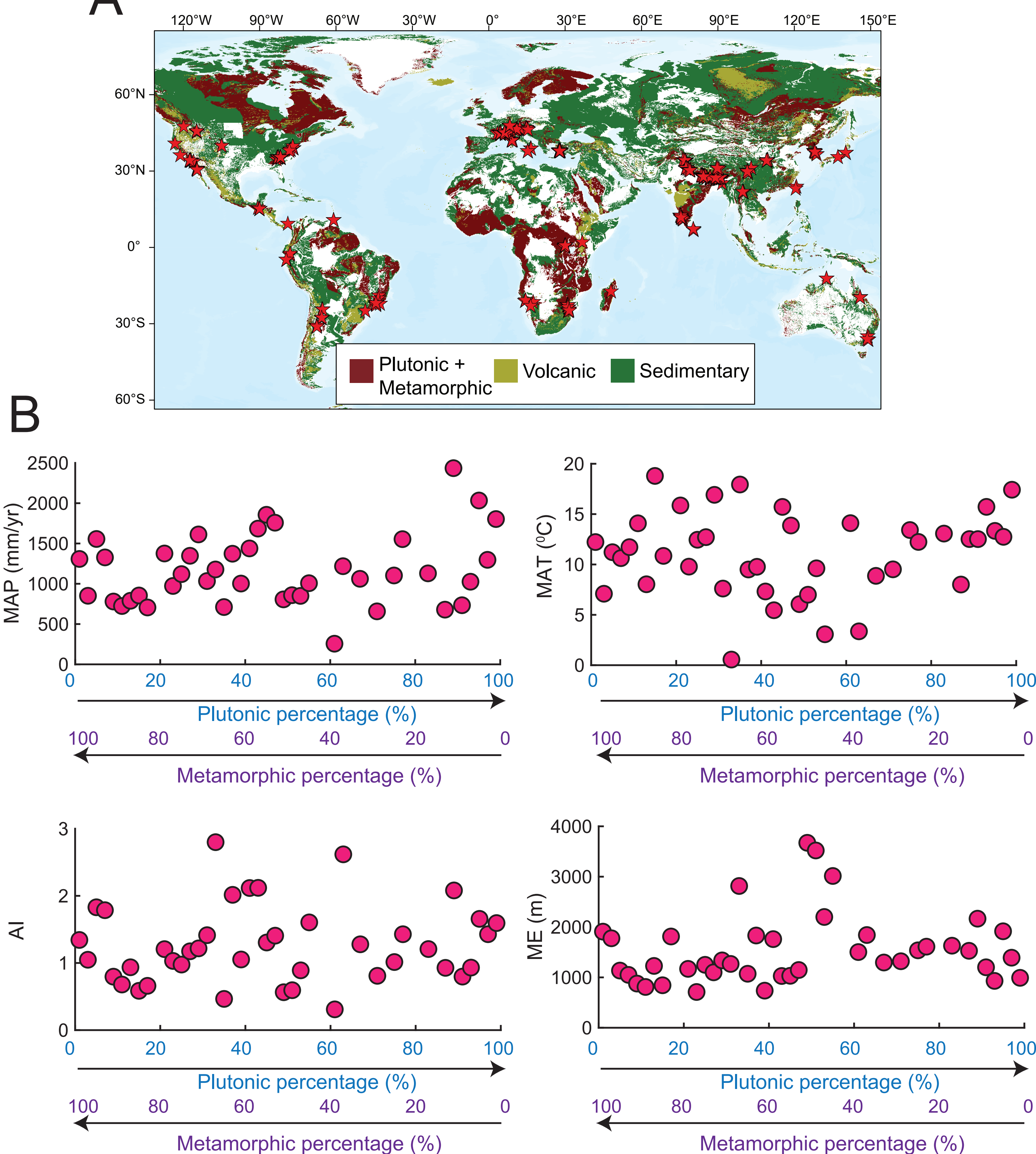
A
120°W
90°W
60°W
30°W
0°
30°E
60°E
90°E
120°E
150°E
60°N
30°N
0°
30°S
60°S
Plutonic + Metamorphic
Volcanic
Sedimentary
B
MAP (mm/yr)
MAT (ºC)
AI
ME (m)
Plutonic percentage (%)
Metamorphic percentage (%)

Fig. S3

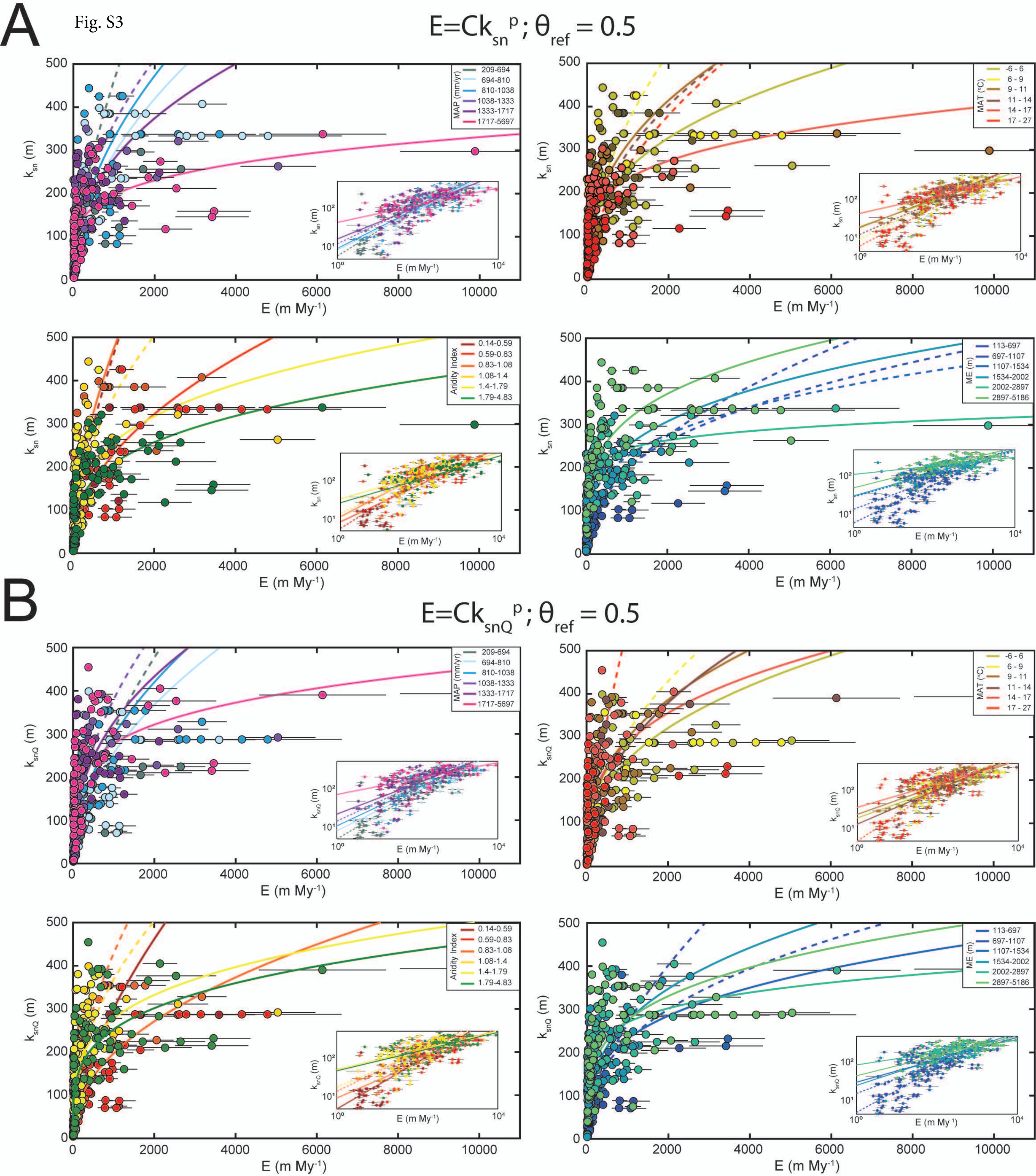

A
E=Ck_sn^p; θ_ref = 0.5
MAP (mm/yr)
209-694
694-810
810-1038
1038-1333
1333-1717
1717-5697
MAT (°C)
-6 - 6
6 - 9
9 - 11
11 - 14
14 - 17
17 - 27
Aridity Index
0.14-0.59
0.59-0.83
0.83-1.08
1.08-1.4
1.4-1.79
1.79-4.83
ME (m)
113-697
697-1107
1107-1534
1534-2002
2002-2897
2897-5186
k_sn (m)
E (m My^-1)
B
E=Ck_snQ^p; θ_ref = 0.5
k_snQ (m)

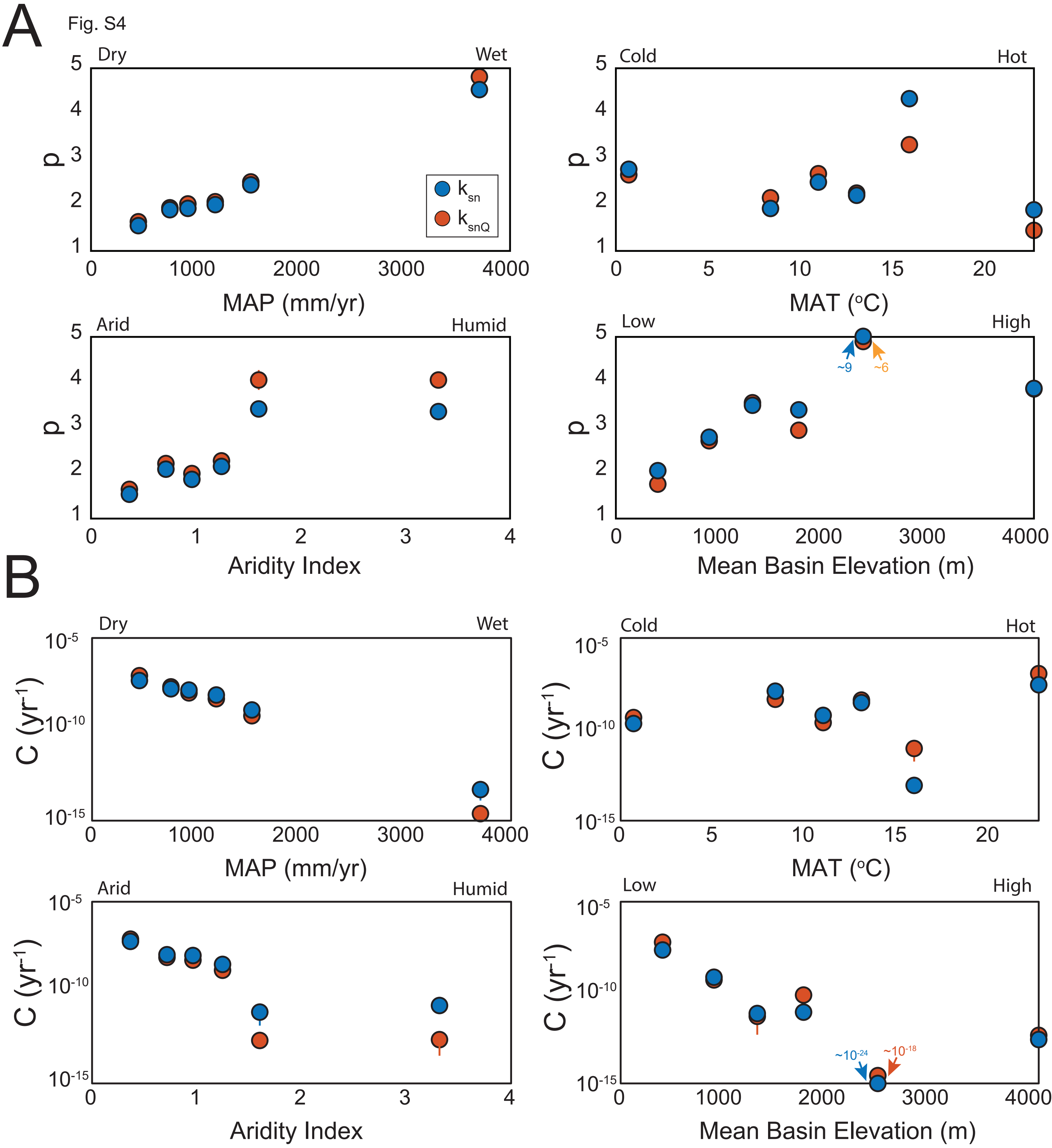
A
Dry
Wet
Cold
Hot
Arid
Humid
Low
High
p
MAP (mm/yr)
MAT (°C)
Aridity Index
Mean Basin Elevation (m)
ksn
ksnQ
~9
~6
B
C (yr-1)
~10-24
~10-18

Fig. S4

Fig. S5

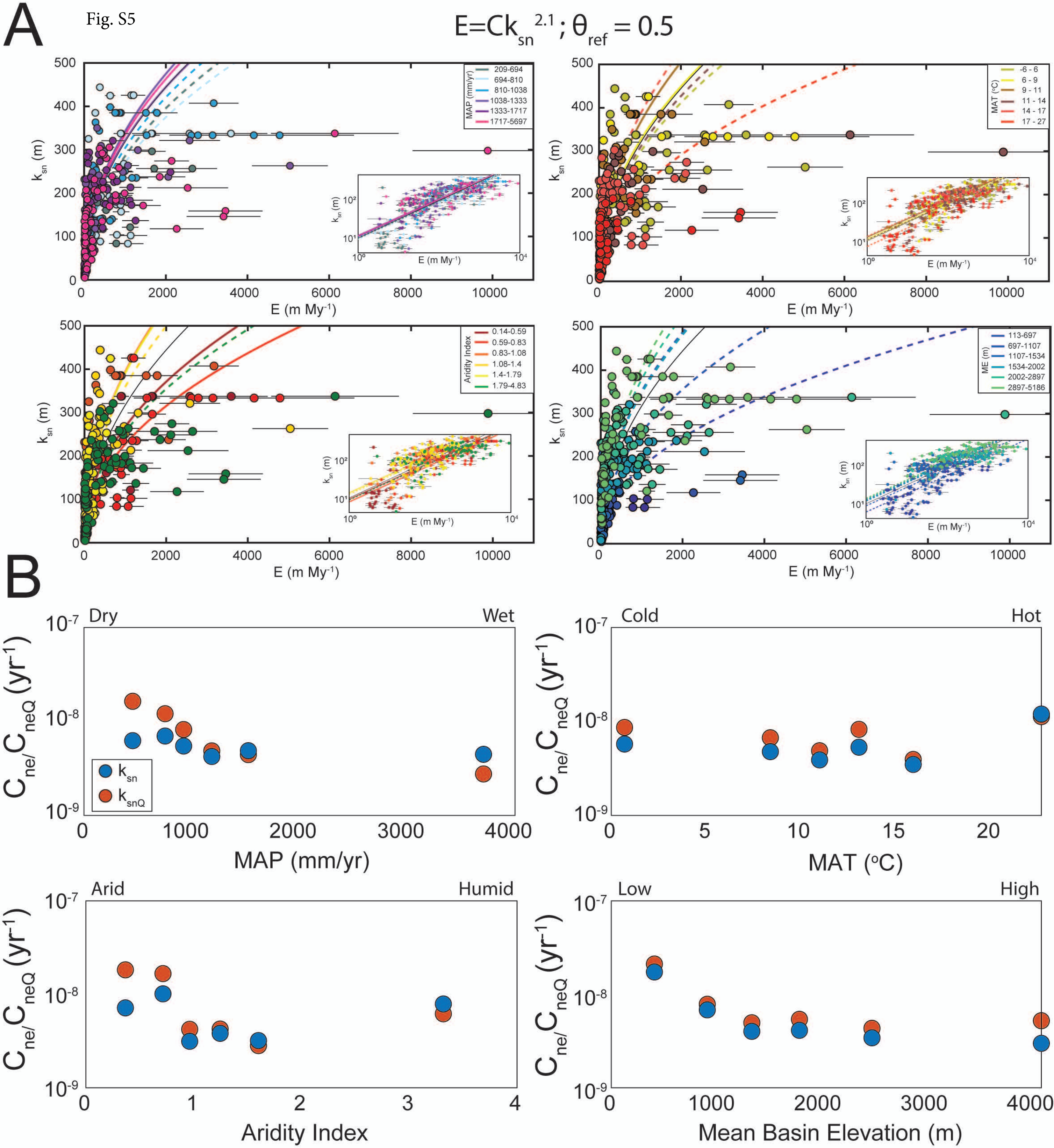

A
$E=Ck_{sn}^{2.1}; \theta_{ref}=0.5$
MAP (mm/yr)
209-694
694-810
810-1038
1038-1333
1333-1717
1717-5697
MAT (°C)
-6 - 6
6 - 9
9 - 11
11 - 14
14 - 17
17 - 27
Aridity Index
0.14-0.59
0.59-0.83
0.83-1.08
1.08-1.4
1.4-1.79
1.79-4.83
ME (m)
113-697
697-1107
1107-1534
1534-2002
2002-2897
2897-5186
k_{sn} (m)
E (m My^{-1})
B
Dry
Wet
Cold
Hot
Arid
Humid
Low
High
C_{ne}/C_{neQ} (yr^{-1})
k_{sn}
k_{snQ}
MAP (mm/yr)
MAT (°C)
Aridity Index
Mean Basin Elevation (m)

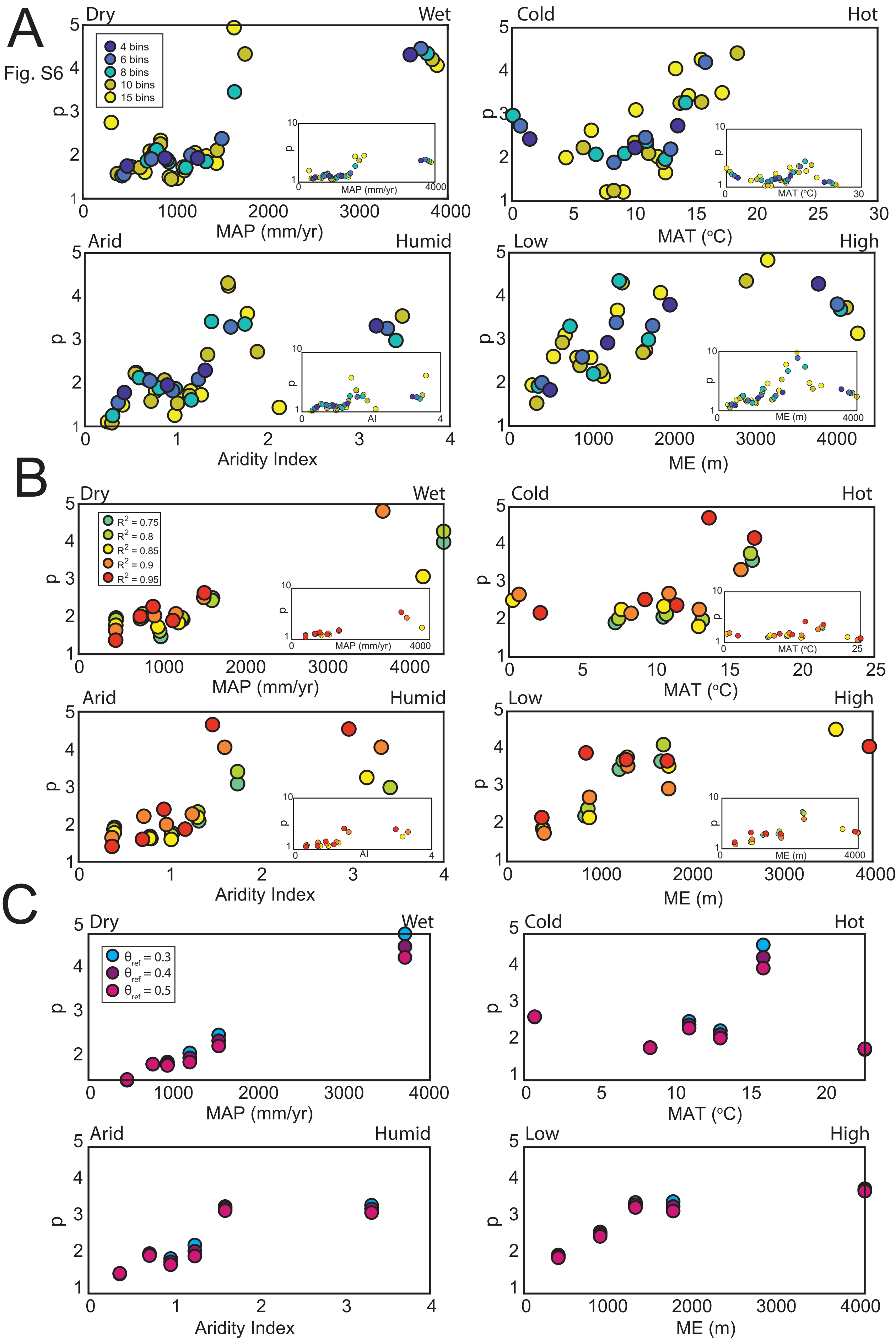

A
Fig. S6
B
C
Dry
Wet
Cold
Hot
Arid
Humid
Low
High
4 bins
6 bins
8 bins
10 bins
15 bins
R^2 = 0.75
R^2 = 0.8
R^2 = 0.85
R^2 = 0.9
R^2 = 0.95
θ_{ref} = 0.3
θ_{ref} = 0.4
θ_{ref} = 0.5
p
MAP (mm/yr)
MAT (°C)
Aridity Index
AI
ME (m)

Fig. S7

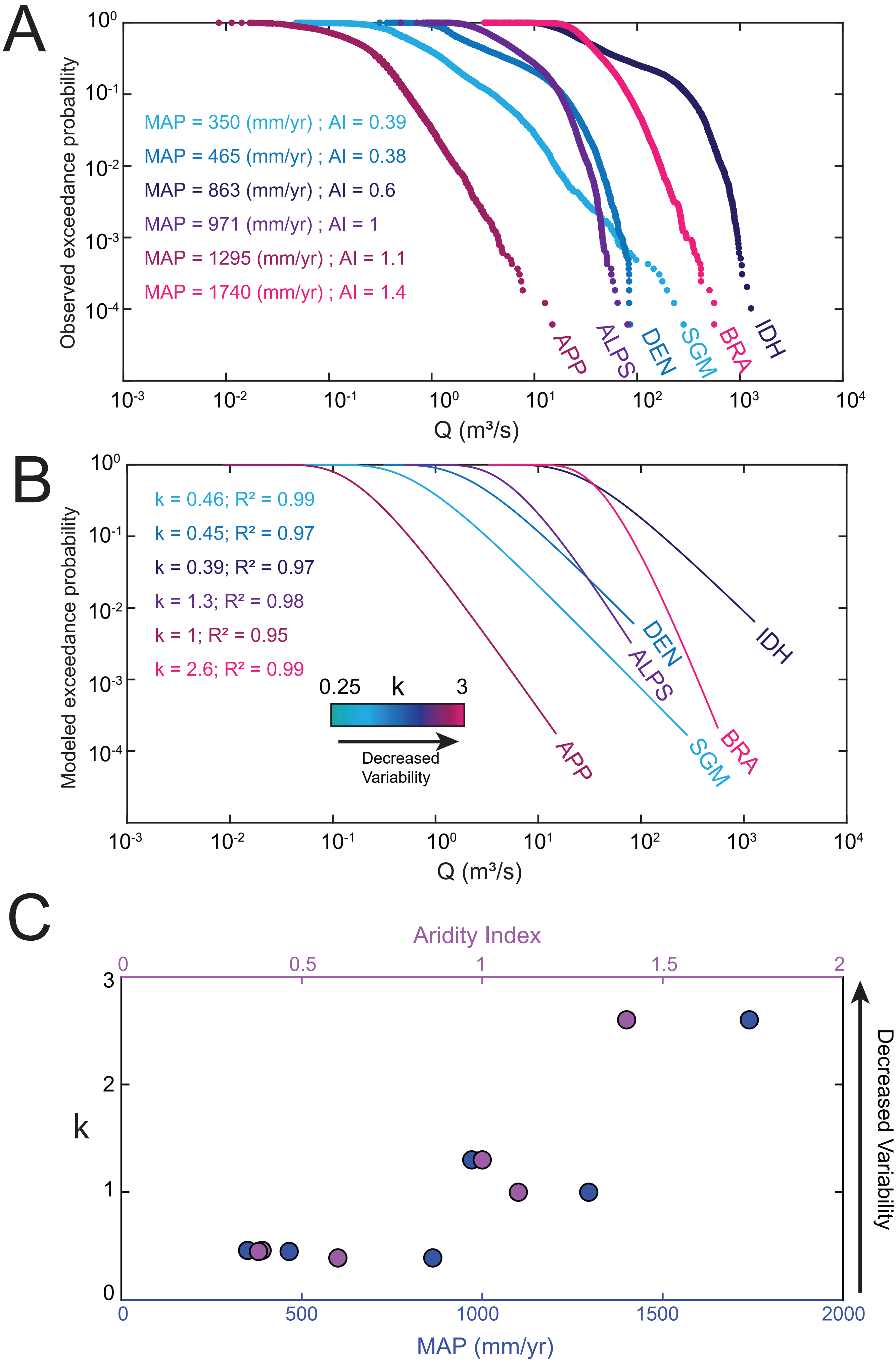

A
Observed exceedance probability
MAP = 350 (mm/yr) ; AI = 0.39
MAP = 465 (mm/yr) ; AI = 0.38
MAP = 863 (mm/yr) ; AI = 0.6
MAP = 971 (mm/yr) ; AI = 1
MAP = 1295 (mm/yr) ; AI = 1.1
MAP = 1740 (mm/yr) ; AI = 1.4
APP
ALPS
DEN
SGM
BRA
IDH
Q (m³/s)
B
Modeled exceedance probability
k = 0.46; R² = 0.99
k = 0.45; R² = 0.97
k = 0.39; R² = 0.97
k = 1.3; R² = 0.98
k = 1; R² = 0.95
k = 2.6; R² = 0.99
0.25
k
3
Decreased Variability
DEN
ALPS
IDH
BRA
SGM
APP
Q (m³/s)
C
Aridity Index
k
Decreased Variability
MAP (mm/yr)